coatings

Article

Fractal Characteristics of Steel–Polypropylene Hybrid Fiber-Reinforced Concrete Under Impact Loading

Qin Zhou [1], Xunda Yang [2,*], Bingyu Weng [2], Jixiang Niu [2] and Xianggang Zhang [2]

[1] School of Spatial Information Engineering, Wuchang University of Technology, Wuhan 430223, China
[2] School of Civil Engineering, Henan Polytechnic University, Jiaozuo 454003, China
* Correspondence: yangxunda17@163.com

Abstract

Natural aggregate concrete is prone to crack propagation and overall crushing under impact load, making it difficult to satisfy the service requirements for collapse resistance in building structures. In order to improve the impact resistance of concrete, this study investigated the impact of the mechanical behavior of steel–polypropylene hybrid fiber-reinforced concrete (SPFRC) using a split Hopkinson pressure bar apparatus. The effects of steel fiber content, polypropylene fiber content, and strain rate on the fractal dimension were examined, and the relationship between total energy dissipation and fractal dimension was established. The results show that the mean fragment size of the crushed specimens decreases linearly with increasing driving voltage, whereas it increases with fiber content. The fractal dimension monotonically increases with an increasing strain rate and decreases as the fiber content increases. Under a driving voltage of 1200 V and steel fiber content of 0.5%, increasing the polypropylene fiber content from 0% to 0.1% yields the largest reduction in the fractal dimension (15.00%) for specimen *S*0.5*P*0.1, exceeding the reductions from increments of 0.1%–0.25% and 0.25%–0.5%. Comparative results demonstrate that SPFRC exhibits superior impact failure resistance compared with concrete reinforced by a mono type of fiber. Exploring the correlation between fractal features and total energy dissipation can realize a more systematic and comprehensive performance assessment of concrete materials. The research results can provide quantitative theoretical support for the impact resistance evaluation and ratio optimization of SPFRC.

Keywords: steel–polypropylene hybrid fiber-reinforced concrete; steel fiber content; polypropylene fiber content; strain rate; fractal dimension; total energy dissipation

Check for updates

Academic Editor: Valeria Vignali

Received: 1 July 2026
Revised: 28 July 2026
Accepted: 29 July 2026
Published: 31 July 2026

1. Introduction

In engineering scenarios such as blast protection, vehicle collision, and mining operations, concrete structures are frequently subjected to short-duration, high-amplitude impact loads. As a typical brittle material, ordinary concrete tends to exhibit abrupt crack propagation and catastrophic fragmentation under such loading, making it difficult to satisfy the service requirements for disaster resistance and risk mitigation in structures [1–4]. For example, local spalling of tunnel linings under vehicle impact and wall cracking in blast-resistant shelters under shock-wave loading are both directly attributable to the insufficient impact toughness of concrete. Therefore, material modification is urgently needed to enhance the dynamic damage resistance of concrete.

At present, researchers have improved the impact resistance of concrete by using new cementitious materials (such as geopolymers) to improve material properties (including

 https://doi.org/10.3390/coatings16080910

the curing ability of harmful elements) [5] and fiber hybrid modification. Fiber hybridization has been recognized as an effective approach to improving the impact performance of concrete. Owing to its high elastic modulus and tensile strength, steel fiber can suppress macrocrack growth through crack-bridging and crack-arrest mechanisms, thereby significantly enhancing the dynamic compressive strength of concrete [6–8]. In contrast, polypropylene fiber exhibits excellent dispersibility and ductility. During the stage of impact loading, energy is dissipated through fiber pull-out, which mitigates the initiation and evolution of microcracks [9–11]. Through the synergistic combination of "rigid strengthening" and "ductile crack control", steel–polypropylene hybrid fiber-reinforced concrete (SPFRC) can achieve improved impact resistance, crack resistance, toughness, and durability. Consequently, SPFRC has the potential to enhance structural safety, extend service life, and promote sustainability in engineering applications [12–14].

Numerous studies have demonstrated the advantages of incorporating hybrid steel and polypropylene fibers into concrete. Arsla [15] conducted drop-weight impact tests on SPFRC to examine crack initiation locations after impact and to evaluate the effects of fiber type and dosage on impact fracture energy. Ren et al. [16] compared the uniaxial compressive response of SPFRC with that of steel fiber-reinforced concrete at high strain rates. They concluded that the hybrid system exhibits superior dynamic mechanical performance. Guo et al. [17] employed quasi-static and dynamic Brazilian splitting tests to investigate the influence of hybrid fibers on the tensile behavior of high-strength concrete. Their results indicated that hybridization increases splitting tensile strength and reduces the risk of brittle failure. Song et al. [18] examined the first-cracking strength, ultimate strength, and strength reliability of SPFRC and compared it with steel-fiber-reinforced concrete, showing that the hybrid system improves the reliability of both first-cracking and ultimate strengths. Guo et al. [19] further evaluated the toughening effects of hybrid fibers in high-strength concrete through flexural tests, quasi-static tests and dynamic splitting tensile tests. The results showed that flexural strength and quasi-static splitting tensile strength are further improved with appropriate dosages of both fibers. In addition, engineering applications such as hydraulic structures and tunnel linings suggest that SPFRC can enhance resistance to abrasion and erosion, thereby reducing maintenance and repair costs. Therefore, systematic investigations into the impact resistance of steel–polypropylene hybrid fiber-reinforced concrete are of practical significance for improving structural safety and advancing construction-material technologies.

However, many meso-damage factors such as micro-voids and microcracks are irregularly distributed inside the SPFRC specimens [20–22]. Under high-velocity impact loading, this micro-damage progressively evolves, propagates, and coalesces, ultimately leading to macroscopic failure. Moreover, within an appropriate observation scale, the fragment distribution and geometrical morphology of post-failure SPFRC are likely to exhibit statistical self-similarity [23–25]. Put forward by Mandelbrot, fractal theory offers a robust analytical framework to characterize irregular geometries and curve features that exhibit statistical self-similarity [26–28]. In essence, concrete impact failure originates from the continuous initiation and expansion of microcracks inside the material to resist impact energy, which eventually evolves into macroscopic damage [29–31]. Subjected to impact loading, concrete fractures into fragments with diverse sizes. On this basis, the fractal dimension can be determined by virtue of the mass–size relationship using fractal theory, which further clarifies the intrinsic relationship between impact mechanical performance and fractal features of SPFRC. Nevertheless, current research predominantly concentrates on how fiber content and strain rate affect macroscopic parameters, like dynamic strength and impact energy dissipation in concrete. Studies adopting fractal theory to reveal the im-

https://doi.org/10.3390/coatings16080910

pact of mechanical behaviors of SPFRC remain scarce; additionally, most researchers merely confine the application of fractal theory to the static performance analysis of concrete.

The scientific reliability and applicability of fractal theory for characterizing irregular failure modes of concrete and quantifying the evolution of material damage have been substantiated by prior studies from multiple perspectives, providing a solid basis for its broader adoption in related areas. By combining machine learning and fractal dimension theory, Szelag et al. [32] performed crack recognition, structural characterization and propagation analysis, clarifying the inherent correlation of the tensile strength of the cement matrix with crack fractal dimension and crack density. Pan et al. [33] distinguished multifractal analysis from monofractal analysis and put forward shape parameters for multifractal spectra. These parameters can quantify the complexity and irregularity of fractal cracks, offering an innovative method for damage evaluation of concrete structures. Based on fracture-mechanics concepts, Carpinteri et al. [34] developed a multiscale fractal method to predict damage evolution and the time to structural collapse. Abdeldjalil et al. [35] developed an innovative quantitative approach. By virtue of the fractal model, the link between the microscopic particle distribution and macroscopic static compressive strength of concrete was established, enabling more precise prediction and optimization of concrete's static mechanical performance. In three-point bending tests of concrete beams, Carpinteri et al. [36] applied the fractal geometry method and established the fractal scaling laws for critical indicators including flexural strength, fracture energy and local rotation. It is demonstrated that such mechanical parameters are not defined based on conventional physical dimensions but on fractal sets of non-integer dimensions. Collectively, the foregoing literature has facilitated the development of fractal theory in concrete engineering regarding crack characterization, performance correlation analysis, and damage prediction. However, current applications of fractal dimensions are largely restricted to crack morphology analysis, with rare expansions to fragment distribution characteristics under impact loading. Notably, the fragment size distribution directly reflects the impact damage degree and can fully characterize the fracture behavior of concrete subjected to dynamic loading.

Motivated by the above, this study systematically investigated the fractal behaviors of SPFRC subjected to impact loading. By implementing SHPB impact tests in combination with fractal theory, the fractal dimension of fragment distribution under various fiber contents and strain rates was quantitatively analyzed. Furthermore, the relationship between fractal dimension and energy dissipation was established, providing quantitative theoretical support for performance evaluation and design optimization of impact-resistant fiber-reinforced concrete structures.

2. Materials and Methods

2.1. Test Materials

Ordinary Portland cement (P·O 42.5, Jiaozuo Qianye Cement Plant, Jiaozuo, China) and high-quality Class I fly ash were used as cementitious materials. The cement had initial and final setting times of 155 and 225 min, respectively; a fineness of 378 m^2/kg; and a loss on ignition (LOI) of 4.27%. Its 3-day compressive and flexural strengths were 31.1 MPa and 6.4 MPa, respectively, meeting the requirements of "Common portland cement" (GB 175–2023) [37]. Fly ash was incorporated at 20% of the cement mass. It had a fineness of 10.3%, a density of 2.3 g/cm^3, a moisture content of 0.08%, and an LOI of 3.03%, complying with "Fly ash used for cement and concrete" (GB/T 1596–2017) [38].

The coarse aggregate was well-graded natural crushed stone with a particle size of 5–10 mm, as shown in Figure 1a. In accordance with "Pebble and crushed stone for construction" (GB/T 14685–2022) [39], it had an apparent density of 2798 kg/m^3, a moisture content of 0.7%, and a water absorption of 0.1%. The coarse aggregate possessed favorable gradation, with the corresponding particle size distribution curve illustrated in Figure 2a. The fine aggregate was natural river sand. According to "Sand for construction" (GB/T 14684–2022) [40], it had an apparent density of 2631 kg/m^3, a bulk density of 1532 kg/m^3, and a fineness modulus of 2.73. The fine aggregate was well graded, and its gradation curve is shown in Figure 2b.

(**a**) Natural coarse aggregate (NCA) (**b**) Steel fiber (**c**) Polypropylene fiber

Figure 1. Coarse aggregate and fiber.

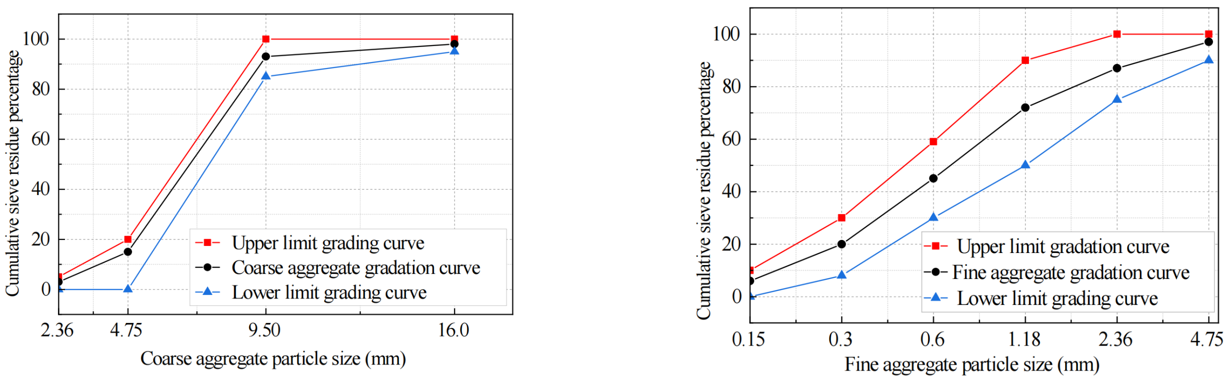

(**a**) Coarse aggregate gradation curve (**b**) Fine aggregate gradation curve

Figure 2. Aggregate grading curve.

A naphthalene-based superplasticizer with a water-reduction rate of 15–25% was used, and its dosage was controlled at 0.5% of the binder mass. The fibers, supplied by Hebei Xisu Engineering Rubber Co., Ltd., Hengshui, China, included copper-coated steel fibers and polypropylene fibers, as shown in Figure 1b,c. The basic mechanical properties of the steel fibers were tested in accordance with "Steel fiber for concrete" (GB/T 39147–2020) [41], while those of the polypropylene fibers were determined following "Man-made fibre—Test method for tensile properties of staple fibre" (GB/T 14337–2022) [42]. The steel fiber used herein possesses a bulk density of 7.85 g/cm^3, a nominal length of 13 mm, and a nominal diameter of 0.2 mm, without tensile fracture occurring at ultimate load. Correspondingly, its tensile strength ranges up to 2965 MPa, elastic modulus varies from 40 GPa to 60 GPa, and Poisson's ratio falls within the range of 0.19–0.24. The polypropylene fiber featured a density of 0.91 g/cm^3, a nominal length of 12 mm, a diameter ranging from 0.018 mm to 0.048 mm, a breaking elongation of 25%, a tensile strength of 560 MPa, and an elastic modulus of 5.18 GPa. The basic mechanical properties of both fibers are summarized in Table 1.

https://doi.org/10.3390/coatings16080910

Table 1. Basic mechanical properties of fiber.

Fiber Type	Density/(g/cm^3)	Length/mm	Diameter/mm	Tensile Strength/MPa	Elastic Modulus/GPa	Poisson's Ratio	Aspect Ratio
Steel fiber	7.85	13	0.2	2965	40–60	0.19–0.24	65
Polypropylene fiber	0.91	12	0.018~0.048	560	5.18	/	250~667

2.2. Mix Proportion

Following the "Specification for mix proportion design of ordinary concrete" (JGJ 55–2011) [43], the tested SPFRC was confirmed to have a C40 strength grade after mix proportion optimization and relevant performance verification. Both steel fibers and polypropylene fibers were incorporated by volume fraction. The steel fiber volume fraction was set at 0%, 0.5%, 1.0%, and 1.5%, while the polypropylene fiber volume fraction was set at 0%, 0.1%, 0.25%, and 0.5%, yielding 16 mix combinations in total. The mix proportion and slump value are listed in Table 2. Specimens were labeled using a "letter + number" convention. For example, "*S*0*P*0.1" denotes a specimen containing 0% steel fiber (*S*0) and 0.1% polypropylene fiber (*P*0.1) by volume. Furthermore, all other specimens follow the same rule.

Table 2. Mix proportion and slump.

Specimen Number	Water (kg/m^3)	Cement (kg/m^3)	Fly Ash (kg/m^3)	NCA (kg/m^3)	Fine Aggregate (kg/m^3)	Steel Fiber (kg/m^3)	Polypropylene Fiber (kg/m^3)	Water Reducer (kg/m^3)	Slump/mm
*S*0*P*0	200	355	71	1206.3	567.7	0	0	2.13	167
*S*0*P*0.1	200	355	71	1206.3	567.7	0	0.91	2.13	151
*S*0*P*0.25	200	355	71	1206.3	567.7	0	2.28	2.13	136
*S*0*P*0.5	200	355	71	1206.3	567.7	0	4.55	2.13	121
*S*0.5*P*0	200	355	71	1206.3	567.7	39	0	2.13	154
*S*0.5*P*0.1	200	355	71	1206.3	567.7	39	0.91	2.13	137
*S*0.5*P*0.25	200	355	71	1206.3	567.7	39	2.28	2.13	121
*S*0.5*P*0.5	200	355	71	1206.3	567.7	39	4.55	2.13	106
*S*1*P*0	200	355	71	1206.3	567.7	78	0	2.13	141
*S*1*P*0.1	200	355	71	1206.3	567.7	78	0.91	2.13	120
*S*1*P*0.25	200	355	71	1206.3	567.7	78	2.28	2.13	102
*S*1*P*0.5	200	355	71	1206.3	567.7	78	4.55	2.13	87
*S*1.5*P*0	200	355	71	1206.3	567.7	117	0	2.13	132
*S*1.5*P*0.1	200	355	71	1206.3	567.7	117	0.91	2.13	109
*S*1.5*P*0.25	200	355	71	1206.3	567.7	117	2.28	2.13	92
*S*1.5*P*0.5	200	355	71	1206.3	567.7	117	4.55	2.13	76

Note: NCA is natural coarse aggregate.

2.3. Specimen Design and Production

To reduce result scatter in the split Hopkinson pressure bar (SHPB) impact tests, standard cubic specimens (150 mm × 150 mm × 150 mm) were prepared for the 16 SPFRC mix proportions in accordance with "Standard for test methods of concrete physical and mechanical properties" (GB/T 50081–2019) [44]. After 28 days of standard curing, core drilling and end grinding were conducted to produce cylindrical specimens with a diameter of 50 mm and a height of 25 mm (height-to-diameter ratio = 0.5). The end-face flatness tolerance was controlled within 0.02 mm, satisfying the dimensional and machining requirements for SHPB testing. Prior to the formal tests, a series of pre-impact trials was performed with reference to the "Standard for test methods of concrete physical and mechanical properties" (GB/T 50081–2019) [44] to determine appropriate driving voltages. This procedure was intended to avoid excessively high voltages that could cause brittle pulverization and prevent valid signal acquisition, as well as overly low voltages that would induce insufficient deformation and fail to reach the intended damage level. Based on repeated pre-impact trials and considering the enhanced impact resistance of the fiber-reinforced specimens, five voltage levels (1000 V, 1100 V, 1200 V, 1300 V, and 1400 V) were selected. For each combination of steel-fiber content, polypropylene-fiber content, and driving voltage, three independent specimens were tested for each condition. The overall test procedure is illustrated in Figure 3. The 28-day mechanical properties of the specimens are shown in Table 3.

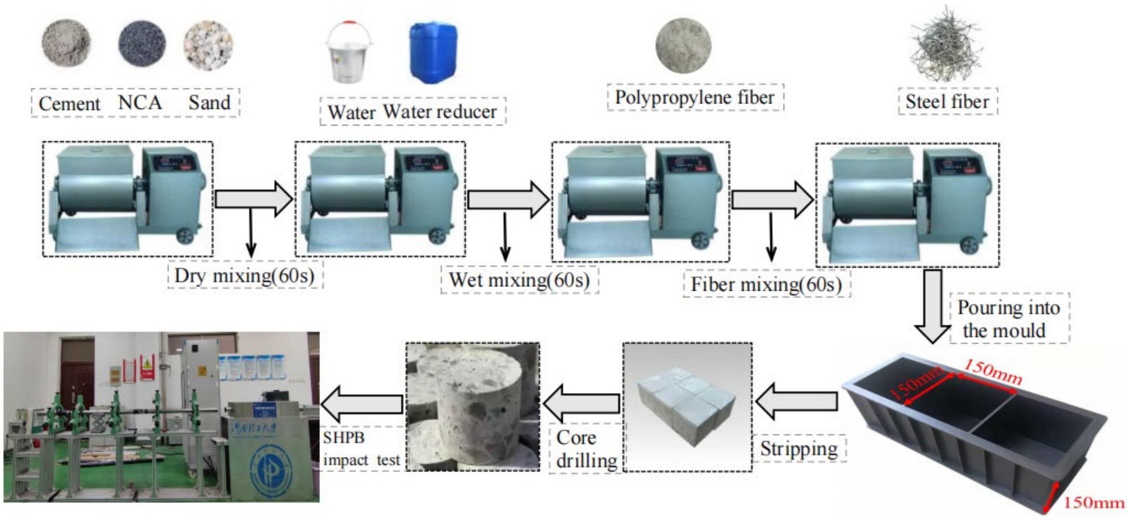

Figure 3. Test process.

Table 3. The measured data of 28-day static performance of steel–polypropylene hybrid fiber-reinforced concrete.

Specimen	f_{cu}/MPa	f_{st}/MPa	Apparent Density/(kg/m^3)	E_c/GPa
*S*0*P*0	40.24	2.72	2420	13.21
*S*0*P*0.1	41.13	2.98	2418	15.69
*S*0*P*0.25	41.96	3.17	2415	16.35
*S*0*P*0.5	42.87	3.30	2412	17.45
*S*0.5*P*0	43.84	3.07	2452	14.56
*S*0.5*P*0.1	44.37	3.29	2450	17.56
*S*0.5*P*0.25	45.16	3.41	2447	18.06
*S*0.5*P*0.5	45.91	3.54	2443	19.45
*S*1*P*0	46.56	3.34	2485	15.71
*S*1*P*0.1	47.33	3.51	2482	18.91
*S*1*P*0.25	48.16	3.66	2479	19.05
*S*1*P*0.5	48.96	3.71	2475	20.71
*S*1.5*P*0	49.69	3.58	2518	17.09
*S*1.5*P*0.1	50.58	3.72	2515	20.72
*S*1.5*P*0.25	51.42	3.84	2511	20.78
*S*1.5*P*0.5	50.14	3.79	2507	20.95

2.4. Test Device and Method

2.4.1. Test Device

An electromagnetically driven SHPB system developed by our research team was utilized in the present study, as illustrated in Figure 4. The electromagnetically driven SHPB system consists of an electromagnetic launching unit, an elastic bar assembly, and a velocity measurement module, as well as a data acquisition and processing system. The electromagnetic launching unit provides the initial kinetic energy required to accelerate the bullet. The launcher barrel has a length of 1000 mm, with an inner diameter of 56 mm and an outer diameter of 60 mm. The control cabinet is equipped with a capacitor bank with a capacitance of 18,000 μF and a rated voltage of 500 V, and the maximum operating voltage of the system can reach 5 kV.

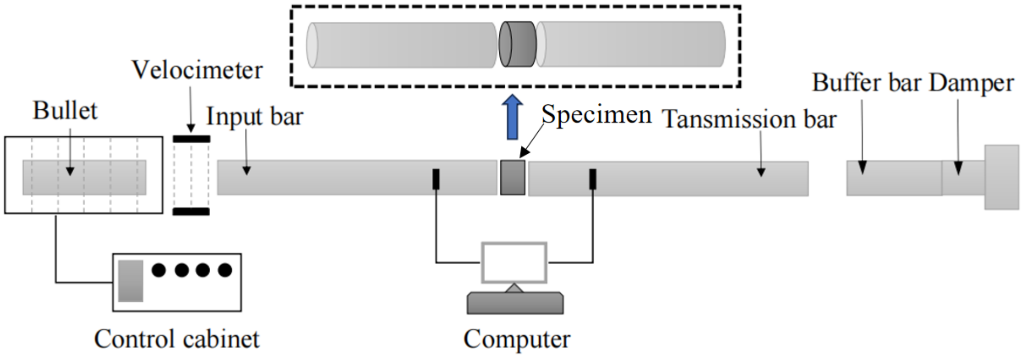

Figure 4. Electromagnetically driven SHPB system.

The elastic bar assembly of the electromagnetically driven SHPB system, which provides the mechanical transmission path for stress waves, comprises an input bar (Φ50 mm × 1000 mm), a transmission bar (Φ50 mm × 1000 mm), and a buffer bar (Φ50 mm × 200 mm). All bars were fabricated from 40Cr alloy steel, with a density of 7930 kg/m^3, a longitudinal wave velocity of 5190 m/s, and an elastic modulus of 210 GPa. As the power unit, the electromagnetic driving system includes a drive coil, a control cabinet, a switching module, and a bullet. The bullet is 400 mm in length and 50 mm in diameter, and it is made of the same alloy steel as the input bar. Following customized surface treatment, three ball bearings were mounted every 100 mm along the surface to lower the frictional resistance between the bullet and the barrel inner wall, which effectively enhances the experimental precision. The data acquisition and processing system consists of a computer, a velocimeter, strain gauges bonded to the bars, and an ultra-high-velocity dynamic strain recorder. These components work together to measure the impact response and determine the dynamic mechanical properties.

2.4.2. Test Method

Before testing, the bullet, input bar, and transmission bar were aligned coaxially to ensure that their axes coincided. The bars were then clamped to restrain vertical displacement while allowing only horizontal motion, thereby ensuring stable stress-wave transmission during impact. Subsequently, high-frequency strain gauges were bonded to the designated locations on the incident and transmission bars, connected to the data acquisition system, and verified through functional checks. Only after confirming normal signal output and the absence of poor electrical contact or gauge damage were the formal tests conducted. Within this test, the collected data include bullet impact velocity, dynamic stress, and strain rates of the specimen.

Initially, the bullet, input bar and transmission bar were coaxially aligned to ensure perfect axial coincidence. The clamps were then secured to constrain vertical bar displacement and permit only horizontal translation, ensuring undisturbed stress wave propagation throughout the impact event. Finally, superconducting strain gauges were mounted at predefined locations on both bars and linked to the data acquisition system for functional checks. The test was initiated only after verifying proper signal output of the strain gauges, with no electrical connection faults or component damage.

Initially, the acquisition parameters were set through the computer of the data acquisition and processing system to prepare for data recording. Subsequently, the main power was connected, and the power and preparation knobs on the front of the control cabinet were activated in sequence. The driving voltage was adjusted to the test design value, followed by closing the rear knife switch to place the circuit capacitors in parallel, thus increasing the total capacity of the energy storage capacitors. Next, the front charging knob was engaged to initiate the charging process. Once the energy storage capacitors were charged to the specified driving voltage, the preparation and charging knobs were deactivated sequentially, and the rear knife switch was opened. The energy storage capacitors then automatically reconfigured into a series of connections to enhance their voltage withstand capability. Finally, the front high-voltage and firing knobs were activated, launching the bullet from the barrel to perform impact loading. Upon test completion, the high-voltage and firing knobs were turned off in reverse order, and the main power was disconnected.

Given the low wave impedance and high brittleness of concrete, copper sheets were adopted as pulse shapers in this test. They were attached to the impact end of the incident bar to prevent the premature end failure of specimens induced by steep incident waves, extend the rising edge of the stress wave, and achieve uniform internal stress distribution within the specimens. All tests were conducted in strict accordance with the one-dimensional stress wave assumption for SHPB tests, and the three-wave method was used to verify the dynamic stress equilibrium for each impact loading. The superposition curve of "incident wave + reflected wave" agreed well with the transmitted wave curve, as shown in Figure 5.

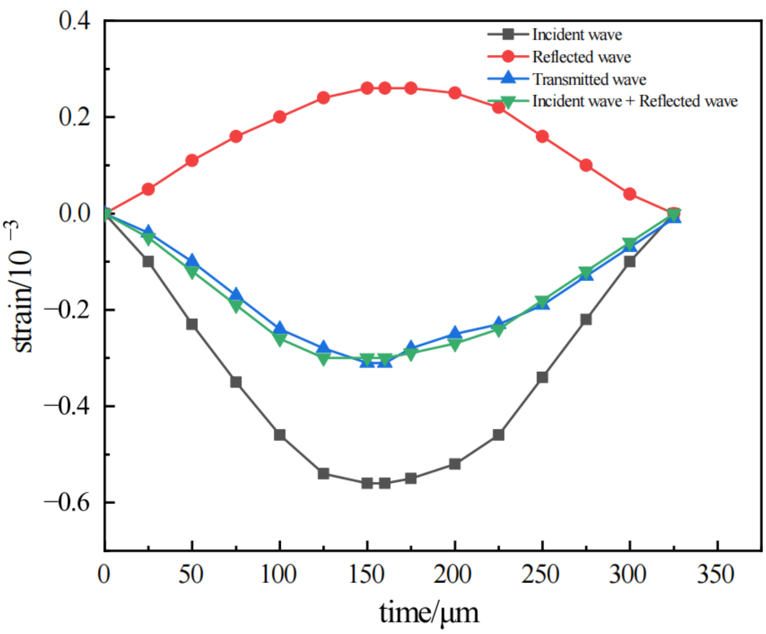

Figure 5. Dynamic stress equilibrium verification.

2.5. Test Principle

The principle of the SHPB test device is based on two basic assumptions:

(1) The one-dimensional elastic wave assumption in the compression bar, that is, the plane assumption: the stress wave is always an elastic wave during the propagation of the bar, and each cross section in the elastic bar always maintains a plane state.

(2) The stress (strain) uniformity of the test block is assumed: during the propagation of the stress wave in the bar, the stress in the test piece is equal everywhere.

According to the one-dimensional elastic stress wave theory, the average stress σ_s, average strain rate $\dot{\varepsilon}_S$, and average strain ε_s of the specimen are obtained, as shown in Equations (1)–(3):

$$\dot{\varepsilon}_S = \frac{C_0(\varepsilon_I - \varepsilon_R - \varepsilon_T)}{L} \quad (1)$$

$$\varepsilon_S = \frac{C_0}{L_S}\int_0^t (\varepsilon_I - \varepsilon_R - \varepsilon_T)dt \quad (2)$$

$$\sigma_S = \frac{E_0 A_0(\varepsilon_I + \varepsilon_R + \varepsilon_T)}{2A_S} \quad (3)$$

where E_0, C_0 and A_0 are the elastic modulus, elastic wave velocity and cross-sectional area of the compression bar, respectively. A_s and L_s are the cross-sectional area and initial length of the sample, respectively. ε_I, ε_R and ε_T represent the incident strain, reflection strain and transmission strain respectively.

According to the assumption of stress uniformity, it can be determined that the forces at both ends of the specimen are equal and agree with Equation (4).

$$F_1 = EA_0(\varepsilon_I + \varepsilon_R) = EA_0\varepsilon_T = F_2 \quad (4)$$

The two sides of the equation are divided at the same time, and Equation (5) is obtained:

$$\varepsilon_I + \varepsilon_R = \varepsilon_T \quad (5)$$

Substituting Equation (5) into Equation (1), the two-wave calculation method is shown in Equations (6)–(8). The data processing in this paper adopts the two-wave method.

$$\dot{\varepsilon}_S = \frac{2C_0(\varepsilon_I - \varepsilon_T)}{L_S} \quad (6)$$

$$\varepsilon_S = \frac{2C_0}{L_S}\int_0^t (\varepsilon_I - \varepsilon_T)dt \quad (7)$$

$$\sigma_S = \frac{EA_0\varepsilon_T}{A_S} \quad (8)$$

Since the cross-sectional area of the strut is the same as the cross-sectional area of the specimen, set to A, the incident energy W_I, reflection energy W_R and transmission energy W_T satisfy Equations (9)–(11) respectively:

$$W_I = AEC_0\int \varepsilon_I^2(t)dt \quad (9)$$

$$W_R = AEC_0\int \varepsilon_R^2(t)dt \quad (10)$$

$$W_T = AEC_0\int \varepsilon_T^2(t)dt \quad (11)$$

According to the law of conservation of energy, the dissipation energy W_D satisfies Equation (12):

$$W_d^{total} = W_I - W_R - W_T \quad (12)$$

3. Results

3.1. Fragment Size Distribution

The fragment size is the most direct quantitative characterization index of the macroscopic crushing degree and damage deterioration degree of the material under impact load, and its value directly reflects the ability of the material to resist impact damage. The smaller the value, the more fully the specimen is broken and the higher the proportion of fine-grained debris, indicating that the more serious the damage caused by the impact load to the material, the worse the impact toughness of the material. The larger the value, the better the overall integrity of the specimen is retained, and the higher the proportion of coarse-grained debris, indicating that the stronger the material's ability to dissipate impact energy, the better the impact resistance.

In the SHPB test, five different driving voltages (1000 V, 1100 V, 1200 V, 1300 V and 1400 V) were used. The experimental data of steel–polypropylene hybrid fiber-reinforced concrete under different fiber content and impact voltage are shown in Table 4. For SPFRC specimens, most retained high structural integrity at driving voltages of 1000 V and 1100 V. In light of this observation, subsequent fractal dimension analysis in this study was limited to SPFRC tested at 1200 V, 1300 V and 1400 V.

Table 4. Impact resistance performance index of steel–polypropylene hybrid fiber-reinforced concrete.

Specimen	Voltage (V)	$\dot{\varepsilon}_0$ (s^{-1})	Specimen	Voltage (V)	$\dot{\varepsilon}_0$ (s^{-1})
*S*0*P*0	800	22	*S*0.5*P*0	1000	42
	900	31		1100	60
	1000	42		1200	77
	1100	58		1300	93
	1200	82		1400	108
*S*0*P*0.1	1000	43	*S*0.5*P*0.1	1000	44
	1100	55		1100	58
	1200	78		1200	73
	1300	87		1300	86
	1400	108		1400	110
*S*0*P*0.25	1000	42	*S*0.5*P*0.25	1000	43
	1100	59		1100	62
	1200	65		1200	71
	1300	72		1300	83
	1400	110		1400	112
*S*0*P*0.5	1000	44	*S*0.5*P*0.5	1000	42
	1100	61		1100	64
	1200	78		1200	76
	1300	87		1300	92
	1400	112		1400	111
*S*1*P*0	1000	43	*S*1.5*P*0	1000	43
	1100	61		1100	63
	1200	79		1200	81
	1300	91		1300	95
	1400	111		1400	109
*S*1*P*0.1	1000	41	*S*1.5*P*0.1	1000	45
	1100	56		1100	60
	1200	75		1200	76
	1300	92		1300	89
	1400	114		1400	113
*S*1*P*0.25	1000	40	*S*1.5*P*0.25	1000	44
	1100	60		1100	61
	1200	76		1200	73
	1300	89		1300	92
	1400	109		1400	106
*S*1*P*0. 5	1000	44	*S*1.5*P*0.5	1000	46
	1100	58		1100	66
	1200	73		1200	79
	1300	91		1300	94
	1400	115		1400	107

Note: $\dot{\varepsilon}_0$ represents the dynamic average strain rate.

The SPFRC fragments produced by high-velocity impact loading were collected in sealed bags and graded through a series of standard sieves with mesh sizes of 2.5, 5, 10, 15, 20 and 50 mm. This yielded six distinct size classes: 0–2.5 mm, 2.5–5 mm, 5–10 mm, 10–15 mm, 15–20 mm and 20–50 mm. The mass of fragments in each size class was then accurately weighed using a high-sensitivity electronic balance and documented.

For SPFRC specimens, most retained high structural integrity at driving voltages of 1000 V and 1100 V. In light of this observation, subsequent fractal dimension analysis in this study was limited to SPFRC tested at 1200 V, 1300 V and 1400 V. The fragment size distribution of SPFRC under varying fiber contents and driving voltages is presented in Figure 6.

Figure 6a–d demonstrate that the fragment size distribution of SPFRC differed significantly with driving voltage. As driving voltage rose, the initial slope of the distribution curve increased, reflecting a gradual reduction in the fraction of coarse fragments (>20 mm) and a corresponding increase in the fraction of fine fragments (<10 mm). Specifically, Figure 6b showed that for specimens with 0.5% steel fiber content and 0.1% polypropylene fiber content, increasing the driving voltage from 1200 V to 1400 V led to a steady decrease in the proportion of coarse fragments (>20 mm) and a steady increase in the proportion of fine fragments (<10 mm), accompanied by a progressive increase in the initial slope of the fragment size distribution curve. In accordance with the fundamental principle of fractal theory, that slope correlates with fractal dimension, this trend indirectly indicated that fractal dimension increased with driving voltage, further validating the well-established relationship that higher impact loads result in more complete specimen fragmentation.

Figure 6e–g demonstrate that the fragment size distribution of SPFRC was significantly influenced by the polypropylene fiber content. Higher polypropylene fiber content led to a progressive reduction in specimen fragmentation severity. Specifically, as shown in Figure 6e, at a constant driving voltage of 1200 V and steel fiber content of 0.5%, increasing the polypropylene fiber content from 0% to 0.5% resulted in a gradual rise in the fraction of coarse fragments (>20 mm). This phenomenon is attributed to the ability of polypropylene fibers to effectively suppress microcrack initiation and branching, which limits the generation of fine fragments and consequently preserves a higher proportion of large fragments.

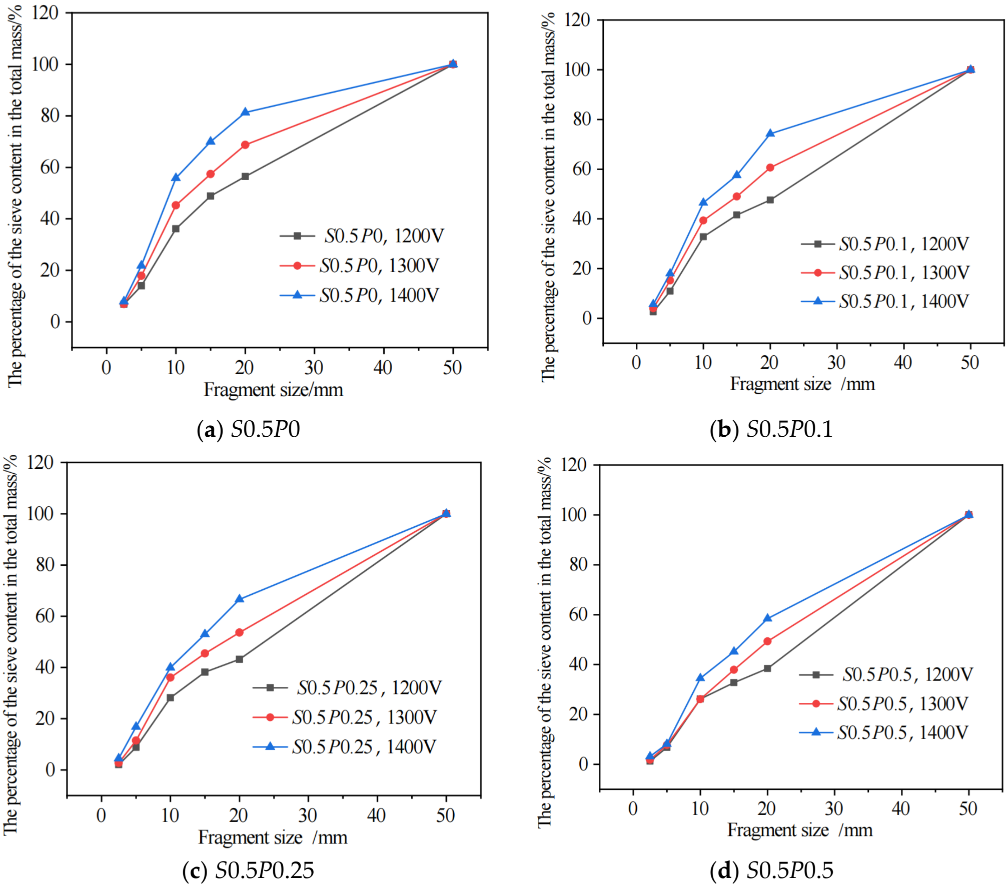

(**a**) *S*0.5*P*0 (**b**) *S*0.5*P*0.1

(**c**) *S*0.5*P*0.25 (**d**) *S*0.5*P*0.5

Figure 6. *Cont.*

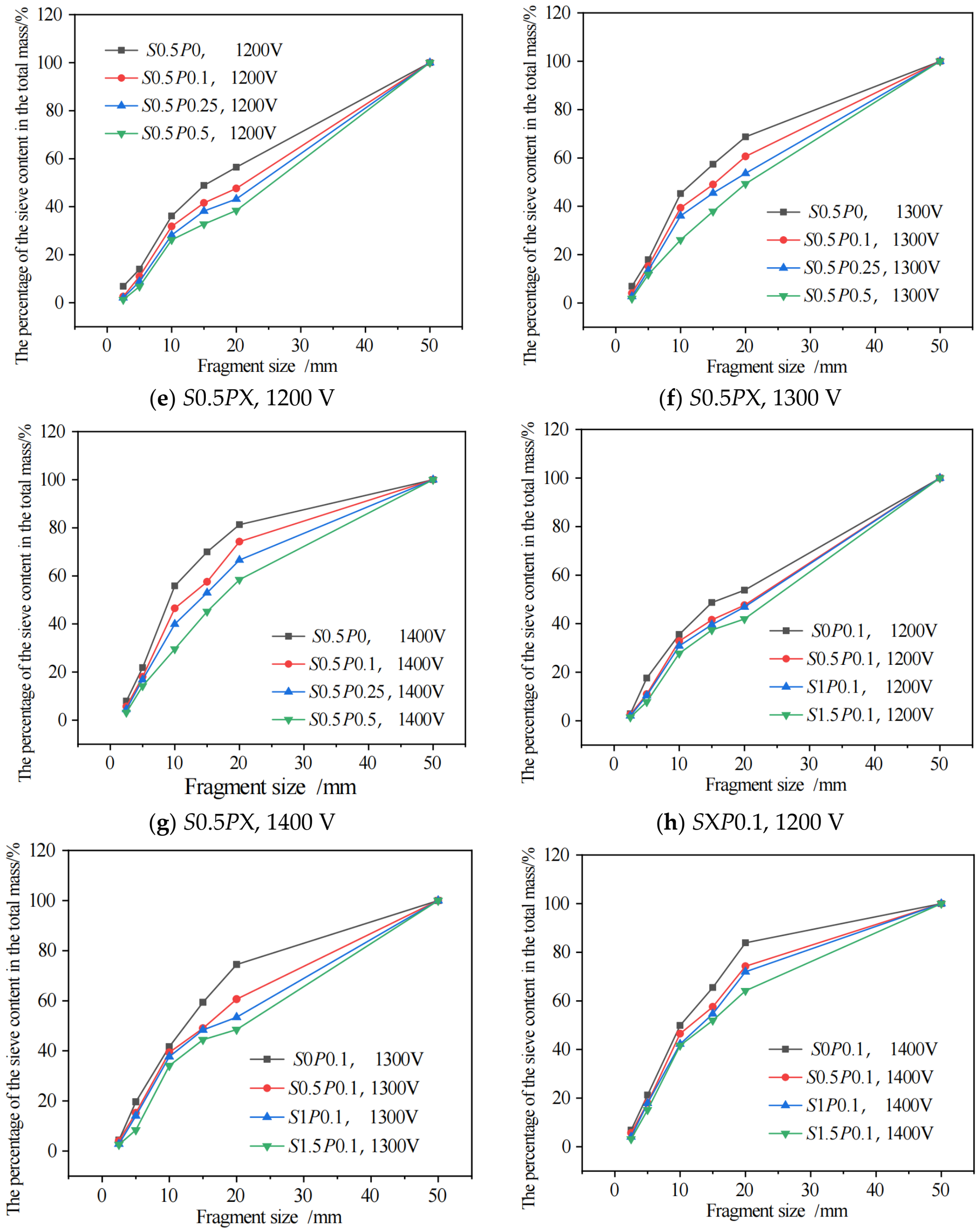

(**e**) *S*0.5*PX*, 1200 V (**f**) *S*0.5*PX*, 1300 V

(**g**) *S*0.5*PX*, 1400 V (**h**) *SXP*0.1, 1200 V

(**i**) *SXP*0.1, 1300 V (**j**) *SXP*0.1, 1400 V

Figure 6. The fragment size distribution of SPFRC specimens under varying parameters. Note: In the subfigure labels S0.5PX and SXP0.1, "X" represents the variable volume fraction of polypropylene fiber and steel fiber, respectively, covering all mixture gradients designed in this study.

Similarly, Figure 6h–j illustrate that steel fiber content also exerted a pronounced effect on the fragment size distribution of SPFRC. Increasing steel fiber content further reduced the overall fragmentation degree of the specimens. As depicted in Figure 6h, at a driving voltage of 1300 V and a fixed polypropylene fiber content of 0.1%, raising the steel fiber content from 0% to 1.5% yielded a comparable increase in the proportion of coarse fragments (>20 mm). This is due to the fact that steel fibers, with their exceptional strength and stiffness, serve as the macroscopic reinforcement skeleton within the concrete matrix, restraining macrocrack propagation and preventing catastrophic overall failure, thereby retaining a greater number of large fragments.

In summary, the experimental results indicate that, regardless of whether SPFRC contains only steel fibers, only polypropylene fibers, or both fibers, the extent of damage gradually decreases with increasing fiber content. This finding confirms that both steel and polypropylene fibers exert a pronounced crack resistance effect on the concrete matrix, which improves specimen integrity under impact loading.

3.2. Calculation of Fractal Dimension of Fragments

Based on the mass–frequency relationship [45–47], the fragment size distribution equation of SPFRC specimens after high-velocity impact loading can be expressed as Equation (13).

$$y = M(r)/M(T) = (r/r_m)^D \tag{13}$$

where r represents the size of the fragment, r_m represents the maximum size of the fragment, D represents the distribution parameter of the fragment, M(r) represents the cumulative mass of the fragment whose size is less than r, and M(T) is the total mass of the fragment.

The fractal dimension D_b of the SPFRC fragment can be expressed according to the linear characteristic size (particle size) r of the fragment and the number of fragments larger than size N [48,49], as shown in Equation (14).

$$N = r^{-D_b} \tag{14}$$

The relationship between the increment in fragment number and the increment in fragment mass is given by Equation (15).

$$\mathrm{d}N \propto r^3 \mathrm{d}M(r) \tag{15}$$

By manipulating Equations (13) and (14) and substituting the results into Equation (15), the fractal dimension of the concrete fragments can be determined, as expressed in Equation (16).

$$D = 3 - D_b \tag{16}$$

Taking the logarithm of both sides of Equation (13) yields:

$$\ln y = \ln[M(r)/M(T)] = (3 - D_b)\ln(r/r_m) \tag{17}$$

Based on Equation (17), the curve of $\ln[M(r)/\mathrm{M}(T)] - \ln r$ was plotted, as shown in Figure 7, where the slope of the curve is $(3 - D_b)$. Figure 7 reveals that the fragment data of SPFRC subjected to high-velocity impact loading display a distinct linear trend in the log–log plot, with a well-fitted correlation. This characteristic stems from the intrinsic coupling between the material fragmentation mechanism and the mathematical fundamentals of fractal theory. From a mathematical perspective, the theoretical equation governing fragment size–quantity relationships becomes linear after logarithmic conversion, closely matching the experimental results and confirming that fragmentation follows deterministic fractal rules instead of random patterns. Mechanistically, steel fibers suppress the penetration of macrocracks via crack bridging, whereas polypropylene fibers restrict microcrack branching and propagation at the mesoscale. Their synergistic action complicates crack growth routes and optimizes energy dissipation, forming a controllable, gradient-continuous orderly fragment distribution. This further reinforces the linear correlation in the log–log domain from a physical perspective [50–52]. The identified fractal properties demonstrate superior self-similarity in fragment distribution, meaning the statistical regularity of fragments holds across different observation scales, delivering valuable guidance for engineering applications. First, fractal parameters obtained from small laboratory specimens can predict the impact fracture performance of full-scale structural components, significantly cutting experimental costs. Second, based on self-similarity, the established correlation model integrating fractal dimension, impact energy level and fiber content enables targeted performance optimization and provides solid theoretical support for the design of impact-resistant concrete structures.

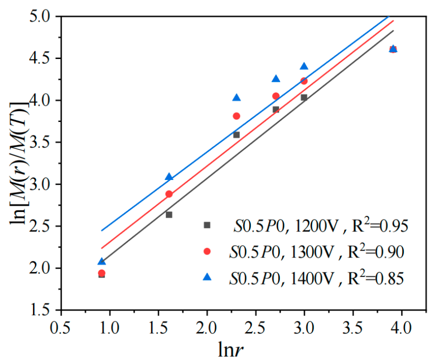

(**a**) $S0.5P0$

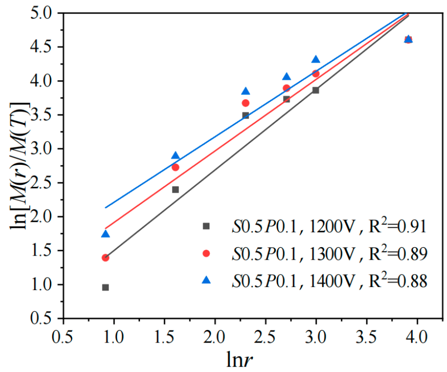

(**b**) $S0.5P0.1$

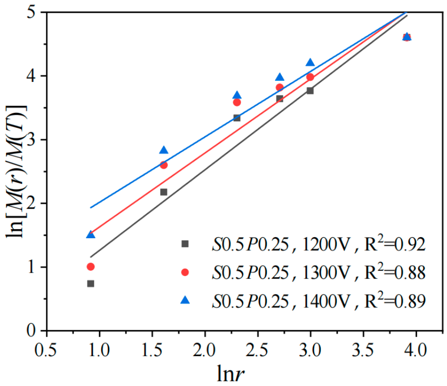

(**c**) $S0.5P0.25$

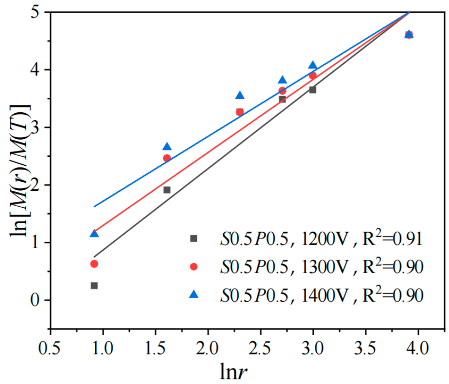

(**d**) $S0.5P0.5$

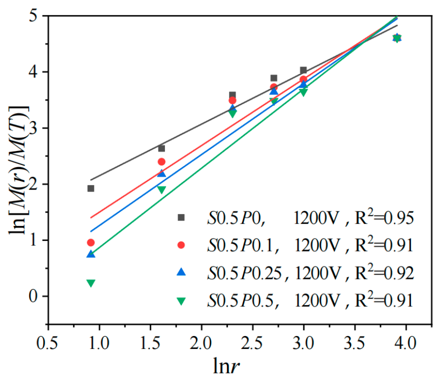

(**e**) $S0.5PX$, 1200 V

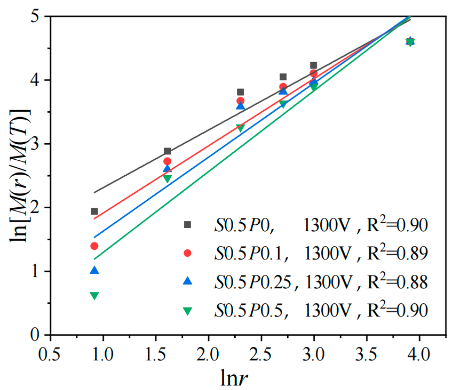

(**f**) $S0.5PX$, 1300 V

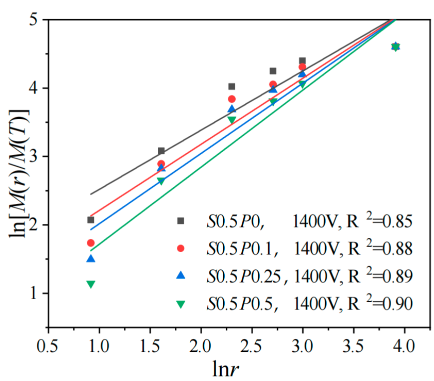

(**g**) $S0.5PX$, 1400 V

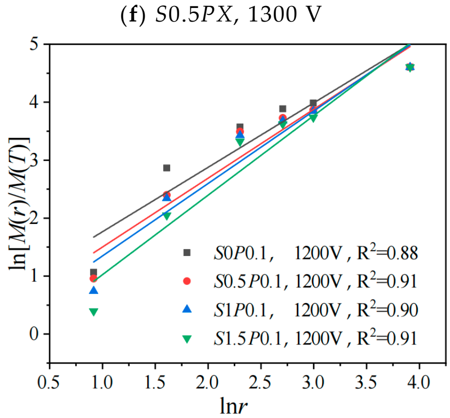

(**h**) $SXP0.1$, 1200 V

Figure 7. *Cont.*

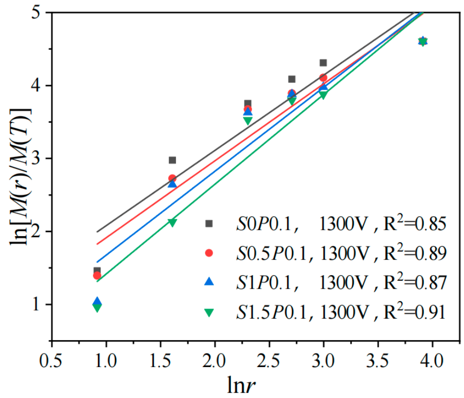

(**i**) $SXP0.1$, 1300 V

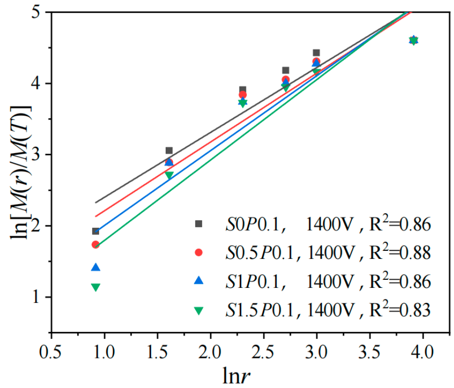

(**j**) $SXP0.1$, 1400 V

Figure 7. $\ln[M(r)/M(T)] - \ln r$ curves of SPFRC specimens with varying parameters. Note: In the subfigure labels S0.5PX and SXP0.1, "X" represents the variable volume fraction of polypropylene fiber and steel fiber, respectively, covering all mixture gradients designed in this study.

The fractal dimension served as a quantitative characterization of the impact crushing degree of the specimen. The increase in fractal dimension indicated that the specimen was more fully broken, the proportion of fine-grained debris was increased, and the initiation and propagation of internal cracks were more thorough. Therefore, the impact damage of the material was more serious, and the impact resistance was weaker. The decrease in the fractal dimension indicates that the overall integrity of the specimen was better retained after failure, the proportion of coarse particle fragments was higher, and the crack propagation was effectively suppressed. Thus, the impact toughness and failure resistance of the specimen were better. Accordingly, the linear correlation in Figure 7 not only experimentally validates fractal theory for characterizing the impact fragmentation behavior of SPFRC but also underpins the full-process closed-loop innovation from theoretical modeling and material optimization to practical engineering implementation. This figure shows the underlying ordered characteristics of SPFRC under dynamic loading; quantifies its macroscopic impact response via a fractal dimension that is describable, predictable and regulable; and significantly advances the intelligent design and application of high-performance anti-impact protective materials.

4. Discussion

4.1. The Influence of Different Parameters on the Fractal Dimension

Figure 8 illustrates the fractal dimension evolution of SPFRC specimens subjected to varied governing parameters. A pronounced increase in fractal dimension was observed with elevated driving voltage, which manifested a typical strain rate-dependent mechanical response. As demonstrated in Figure 8c, for specimen $S1.5P0.25$, successive increases in driving voltage from 1200 V to 1300 V and further to 1400 V induced fractal dimension increments of 11.48% and 7.65%, respectively. Notably, $S1.5P0.25$ yielded the highest fractal dimension growth rate (11.48%) among all tested specimens in Figure 8c upon progressive driving voltage enhancement. Similarly, in Figure 8e, the fractal dimension of specimen $S0P0.5$ rises by 11.45% and 5.41% at driving voltages of 1200 V, 1300 V and 1400 V. Within the specimen group of Figure 8e, $S0P0.5$ presents the maximal fractal dimension amplification (11.45%) with the gradual elevation of driving voltage. This phenomenon originates from the enhanced impact velocity induced by higher driving voltage. Under dynamic impact loading, rapid propagation and proliferation of internal microcracks occur instantaneously within the concrete matrix, exacerbating specimen fragmentation. The resultant reduction in fragment size and increase in fragment quantity collectively contribute to the elevation of fractal dimension. The findings of the present work are in excellent agreement with the conclusions drawn from the extensive prior literature [53–55].

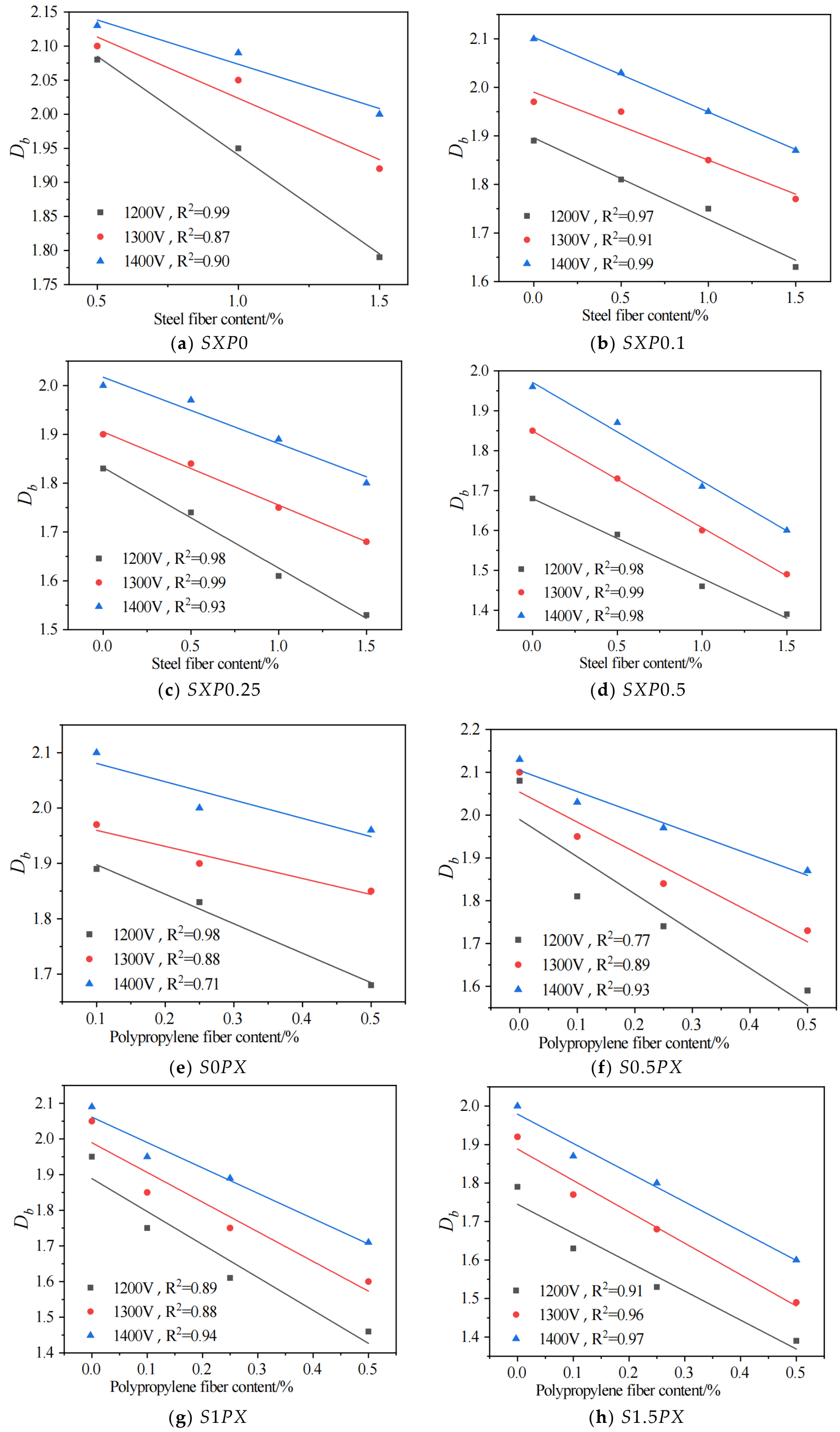

Figure 8. Relationship curves between varying parameters and fractal dimension. Note: In the (**a**–**d**), "X" represents the variable volume fraction of steel fiber and in the (**e**–**h**), "X" represents the variable volume fraction of polypropylene fiber, covering all mixture gradients designed in this study.

Figure 8a–d reveal that the fractal dimension declined with elevated steel fiber content under fixed polypropylene fiber content and constant driving voltage. Considerable decreases in fractal dimension were identified at polypropylene fiber additions of 0% and 0.5%. As illustrated in Figure 8a, for mono steel-fiber-reinforced specimens subjected to 1200 V, 1300 V and 1400 V, the fractal dimension decreased in the ranges of 6.41%–9.55%, 2.38%–6.34% and 2.35%–3.85% with increasing steel fiber content. At 1200 V and 0% polypropylene fiber content, specimen *S*1.5*P*0 achieved the maximum fractal dimension reduction (9.55%) when steel fiber content increased from 1.0% to 1.5%, which surpassed the reduction induced by the content increment from 0.5% to 1.0%. In Figure 8d, with constant driving voltages (1200 V, 1300 V, 1400 V) and fixed polypropylene fiber content of 0.5%, the fractal dimension drops by 3.57%–8.97%, 6%–8.23% and 4.62%–7.53% as steel fiber content increases. Notably, at 1200 V and 0.5% polypropylene fiber content, specimen *S*1*P*0.5 exhibited a marked fractal dimension reduction of 8.97% during the steel fiber content increase from 0.5% to 1.0%, outperforming all other gradual content-varying stages. This phenomenon stems from the dual enhancement mechanism of steel fibers: structural framework construction and mechanical property optimization, which effectively preserves the structural integrity of concrete under dynamic impact loading. On the one hand, randomly dispersed steel fibers build an interlaced network within the concrete matrix, restraining tensile crack propagation and providing intrinsic structural support for dynamic impact resistance. On the other hand, benefiting from their exceptionally high strength and stiffness, steel fibers constitute a macroscopic load-bearing skeleton inside concrete, further reinforcing the dynamic anti-impact resistance of the hybrid fiber composite. The findings of the present work are in excellent agreement with the conclusions drawn from the extensive prior literature [56–58].

Figure 8e–h demonstrate that for fixed steel fiber content and constant driving voltage, the fractal dimension declined monotonically with the elevation of polypropylene fiber content. Remarkable reductions in fractal dimension were detected at steel fiber additions of 0.5% and 1.0%. As illustrated in Figure 8f, under standardized driving voltages (1200 V, 1300 V, 1400 V) and a constant steel fiber content of 0.5%, the fractal dimension of specimens decreased within the ranges of 6.98%–15.00%, 5.46%–6.15% and 3.43%–5.08% with progressive increases in polypropylene fiber content. At 1200 V coupled with 0.5% steel fiber incorporation, specimen *S*0.5*P*0.1 achieved the most prominent fractal dimension degradation (15.00%) during the polypropylene fiber content increment from 0% to 0.1%, which surpassed the degradation induced by content increments of 0.1%–0.25% and 0.25%–0.5%. Likewise, in Figure 8g, with invariant impact voltages (1200 V, 1300 V, 1400 V) and a fixed steel fiber content of 1.0%, the fractal dimension drops by 9.38%–11.43%, 5.14%–11.41% and 1.95%–8.47% as polypropylene fiber content increased. Notably, at 1200 V and 1.0% steel fiber content, specimen *S*1*P*0.1 presented the maximum fractal dimension reduction (11.43%) when polypropylene fiber content rose from 0% to 0.1%, outperforming the reduction magnitudes in the content transition stages of 0.1%–0.25% and 0.25%–0.5%. This underlying mechanism can be elaborated as follows: relying on superior tensile confinement and interfacial adhesion, polypropylene fibers efficiently inhibit the initiation and bifurcation of microcracks under dynamic impact loading, avoiding the fragmentation of specimens into fine particles resulting from the coalescence of pervasive microcracks. Meanwhile, the favorable dispersion property of polypropylene fibers enables the formation of a homogeneous transitional coating surrounding steel fibers. Such a transitional layer mitigates stress concentration at the fiber–matrix interface, optimizes the interfacial bonding integrity, and facilitates the macroscopic anticracking performance of steel fibers. Ultimately, a favorable synergistic mechanism integrating microcrack regulation and interfacial modification is established in the hybrid fiber system. The above observed results are consistent with the conclusions drawn from the extensive prior literature [59,60].

Figure 8 revealed that SPFRC possessed markedly enhanced dynamic impact resistance over mono-fiber-reinforced concrete. As evidenced by Figure 8d,e, at constant driving voltages of 1200 V, 1300 V and 1400 V, the fractal dimension of hybrid fiber specimen *S*1.5*P*0.5 was lowered by 20.51%, 24.01% and 21.74%, respectively, compared with the mono polypropylene fiber specimen *S*0*P*0.5. Likewise, in Figure 8g,h, under fixed driving voltages and a total fiber content of 1.5%, specimen *S*1*P*0.5 exhibits fractal dimension reductions of 25.17%, 20.00% and 12.86% relative to mono steel fiber specimen *S*1.5*P*0. Hybrid fiber systems maintain a persistently lower fractal dimension than mono fiber configurations, and a reduced fractal dimension quantitatively reflects superior dynamic impact performance of concrete composites. For mono steel-fiber-reinforced specimens, steel fibers mitigate crack-tip stress concentration and arrest crack propagation during fracture evolution, attributed to robust interfacial adhesion between fibers and cementitious matrix. This mechanism has been well documented in prior investigations [61–63]. In contrast, mono polypropylene-fiber-reinforced concrete presents a distinct anti-fracture behavior: upon microcrack initiation, polypropylene fibers undergo substantial tensile elongation as cracks develop, with their bearing capacity progressively elevated. The crack diversion effect disperses dominant macrocracks into dense microcracks, effectively retarding crack growth. This inference aligns with published research outcomes [64–66]. The excellent impact resistance of hybrid fiber concrete stems from the synergistic reinforcement of dual fibers. Randomly oriented steel and polypropylene fibers construct a cross-linked three-dimensional network throughout the matrix, enabling multiscale inhibition of tensile fracture. High-modulus steel fibers dominate the control of early-stage crack initiation and propagation, whereas ductile polypropylene fibers improve post-fracture deformability and energy dissipation. Their complementary reinforcement establishes a powerful confinement effect, achieving prominent enhancement in dynamic impact performance. The above inferences are consistent with the systematic previous studies [67–69]. Overall, mono steel fibers function to relieve stress concentration and restrain crack extension, mono polypropylene fibers disperse macrocracks via crack diversion, and hybrid fibers realize integrated complementary reinforcement relying on the three-dimensional interwoven network structure.

4.2. The Relation Between Fractal Dimension and Total Energy Dissipation of SPFRC Specimens Under Varying Parameters

Figure 9 depicts the correlation between fractal dimension and total energy dissipation of SPFRC. The computational approach for total energy dissipation followed the documented methods in our group's published literature [70,71]. For each curve in Figure 9a–d, the parameter U_n corresponds to 1200 V, 1300 V, and 1400 V in sequence from left to right; for Figure 9e–g, the parameter *X* is defined as 0, 0.1, 0.25, and 0.5 along each curve. In Figure 9e–g, specimen *S*0*P*0 exhibits typical powdery failure, lacking valid morphological features and qualified data for quantitative analysis. Hence, for the *S*0*PX* specimen series, *X* was designated as 0.1, 0.25 and 0.5. With fixed steel and polypropylene fiber contents, elevated driving voltage contributed to synchronous growth in total energy dissipation and fractal dimension. As demonstrated in Figure 9d, for specimen *S*1.5*P*0.25, incremental increases in driving voltage from 1200 V to 1300 V and further to 1400 V caused total energy dissipation to rise by 20.22% and 27.27%, with the fractal dimension increasing by 7.65% and 11.48%, respectively. The voltage increase from 1300 V to 1400 V yielded the highest growth rates for both total energy dissipation (27.27%) and fractal dimension (11.48%) in specimen *S*1.5*P*0.25. This phenomenon originates from the transient nature of dynamic impact loading, which distinguishes crack evolution from that under static loading conditions. Massive microcracks are initiated throughout the matrix, rather than the propagation of one dominant crack or several discrete cracks. The initiation and growth of new cracks derived from internal defects inevitably consume additional fracture energy. Consequently, higher impact excitation triggers extensive microcrack generation and deeper penetration within an ultra-short loading period, resulting in the simultaneous enhancement of fractal dimension and energy dissipation capacity. The present conclusions are in excellent agreement with widespread previous research outcomes [35,36,72].

For a given driving voltage and polypropylene fiber content, elevating the steel fiber content induced a progressive rise in total energy dissipation and a monotonic decline in fractal dimension. The most pronounced enhancement in energy consumption and reduction in the fractal dimension was observed at the driving voltage of 1400 V with increasing steel fiber incorporation. At 0.25% polypropylene fiber content, the maximum growth rate of total energy dissipation (12.71%) was obtained in specimen *S*1*P*0.5 when the steel fiber content rose from 0.5% to 1.0%, which outperformed the increments from 0% to 0.5% and 1.0% to 1.5%. For specimens with 0.5% polypropylene fiber content, the steel fiber content increase from 1.0% to 1.5% contributed to the largest fractal dimension reduction (8.11%) in *S*1.5*P*0.5, surpassing the effects of other content transition stages. As illustrated in Figure 9g, at a constant driving voltage of 1400 V and polypropylene fiber contents of 0%, 0.1%, 0.25% and 0.5%, the total energy dissipation increased in the ranges of 4.35%–5.22%, 8.48%–9.27%, 7.27%–12.71% and 4.01%–7.76% with increasing steel fiber content. Correspondingly, the fractal dimension decreased by 2.35%–4.33%, 1.92%–4.90%, 1.50%–7.37% and 5.61%–8.11%. This inherent mechanism originates from the fiber–matrix synergistic framework established by steel fibers within the concrete matrix. Such a framework realizes effective stress transfer and dispersion to avoid catastrophic brittle failure, while additional fracture energy is dissipated via fiber pull-out or fracturing; higher fiber content further amplifies this energy dissipation effect. Moreover, steel fibers suppress random crack propagation and regularize crack development paths. They also modify the failure characteristic from brittle splitting fracture to ductile damage, which fundamentally reduces the fractal dimension of fractured concrete.

For a fixed driving voltage and steel fiber incorporation, progressive addition of polypropylene fiber led to a continuous growth in total energy dissipation and a monotonic decline in fractal dimension. The enhancement of energy consumption was particularly prominent at the impact driving of 1400 V with increasing polypropylene fiber content. Notably, at a steel fiber content of 1.5%, the maximum energy dissipation growth rate (10.42%) was recorded for specimen *S*1.5*P*0.1 during the polypropylene fiber content increment from 0% to 0.1%, which surpassed the increments induced by content transitions of 0.1%–0.5% and 0.25%–0.5%. At 1300 V driving voltage, the most pronounced reduction in fractal dimension was observed with the elevation of polypropylene fiber content. For specimens containing 1.5% steel fiber content, the polypropylene fiber content increase from 0.25% to 0.5% yielded the largest fractal dimension drop (11.52%) in specimen *S*1.5*P*0.5, outperforming all other content variation stages. As demonstrated in Figure 9g, under a constant driving voltage of 1400 V and steel fiber contents of 0%, 0.5%, 1%, and 1.5%, the total energy dissipation increased within the ranges of 5.45%–7.32%, 2.75%–5.93%, 5.38%–7.00%, and 7.55%–10.42% with rising polypropylene fiber content. Correspondingly, the fractal dimension decreased by 2.00%–3.85%, 4.23%–6.86%, 2.06%–10.53%, and 5.38%–10.23%. In addition, in Figure 9f, at 1300 V, coupled with steel fiber contents of 0%, 0.5%, 1%, and 1.5%, the total energy dissipation rises by 0.84%–3.48%, 2.50%–3.99%, 3.11%–7.08%, and 2.45%–4.16% as polypropylene fiber content increases. Meanwhile, the fractal dimension presents reductions of 2.30%–3.14%, 6.04%–7.14%, 3.85%–10.78%, and 2.63%–11.52%, respectively.

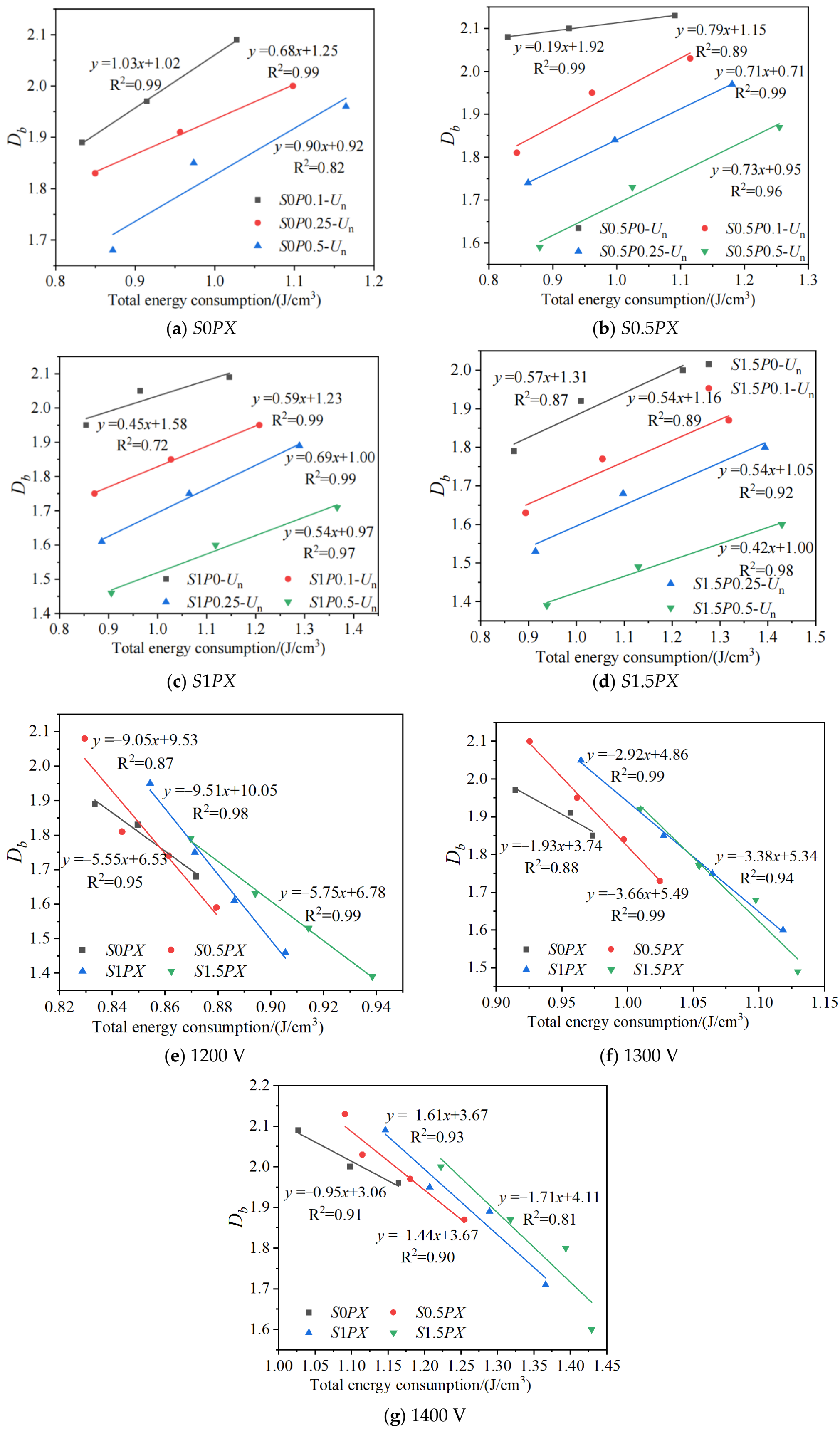

Figure 9. Relationship between total energy dissipation and fractal dimension. Note: In the Figure 9a–d, "X" represents the variable volume fraction of polypropylene fiber, covering all mixture gradients designed in this study.

This underlying mechanism can be elaborated as follows: polypropylene fiber incorporation merely multiplies crack quantity; more importantly, it reshapes the crack evolution pathway via the synergistic crack-arresting and fiber-bridging effects. Under dynamic impact loading, the potential formation of one or two dominant penetrating macrocracks is suppressed, which are further segmented into dense, short, slender, non-penetrating microcracks by distributed polypropylene fibers. The above phenomenological observations agree well with the conclusions drawn from the abundant published literature [73,74]. The propagation of microcracks necessitates persistently overcoming the fiber–matrix interfacial adhesion and the intrinsic bridging stress provided by polypropylene fibers, which consumes considerable dynamic impact energy. Consequently, the energy dissipation capability of the composite is progressively enhanced with elevated polypropylene fiber content. From the perspective of fracture morphology, the fractal dimension quantitatively describes the complexity of the crack network; a higher value corresponds to more branched and randomly distributed cracks. The fiber-bridging action effectively restricts irregular crack bifurcation and disordered propagation. Although numerous microcracks emerge within the matrix, they generally present a short and linear configuration without chaotic branching, maintaining the overall structural integrity of specimens in a typical cracked but non-disintegrated state. Overall, the addition of polypropylene fibers contributes to improved energy dissipation performance and a decreased fractal dimension.

5. Conclusions

Based on fractal theory, this study performed SHPB impact tests on SPFRC and focused on the fractal characteristics of impact-induced fragment size. The main conclusions are summarized as follows:

(1) For mono-steel-fiber-, mono-polypropylene-fiber-, and hybrid fiber-reinforced specimens, the extent of fragmentation declines progressively with elevated fiber content, accompanied by an increased proportion of coarse fragments above 20 mm. The synergistic crack inhibition of steel and polypropylene fibers within the matrix effectively improves the structural wholeness of fractured specimens.

(2) Under constant fiber contents, both the fractal dimension and total energy dissipation grow monotonically with the increase in driving voltage. The most prominent increments in total energy dissipation (27.27%) and fractal dimension (11.48%) are identified in specimen *S*1.5*P*0.25 when the driving voltage is raised from 1300 V to 1400 V, demonstrating a distinct strain rate-dependent mechanical response.

(3) Hybrid fiber reinforcement maintains a lower fractal dimension than mono-fiber reinforcement; such a lower fractal dimension quantitatively reflects the outstanding dynamic impact resistance of hybrid fiber concrete composites.

(4) The fractal dimension decreases with increasing steel fiber content at a fixed polypropylene fiber content and driving voltage. The maximum fractal dimension degradation of 9.55% is captured in *S*1.5*P*0 during the steel fiber increase from 1.0% to 1.5% at 1200 V and zero polypropylene fiber addition. Similarly, increasing polypropylene fiber content reduces the fractal dimension under identical driving voltage and steel fiber content; the peak reduction of 15.00% is found in *S*0.5*P*0.1 with polypropylene fiber rising from 0% to 0.1% at 1200 V and 0.5% steel fiber content.

(5) Higher steel fiber content contributes to enhanced energy dissipation and reduced fractal dimension under specified driving voltage and polypropylene fiber content. At 1400 V and 0.25% polypropylene fiber content, the maximum energy dissipation growth (12.71%) is achieved in *S*1*P*0.25 with steel fiber content increasing from 0.5% to 1.0%. At 1400 V and 0.5% polypropylene fiber content, peak fractal dimension reduction (8.11%) occurs in *S*1.5*P*0.5 as steel fiber content rises from 1.0% to 1.5%.

https://doi.org/10.3390/coatings16080910

(6) Elevated polypropylene fiber content also promotes energy dissipation and suppresses fractal dimension growth with fixed driving voltage and steel fiber content. At 1.5% steel fiber content and 1400 V, *S*1.5*P*0.1 exhibits the highest energy dissipation increment (10.42%) when polypropylene fiber content increases from 0% to 0.1%. At 1.5% steel fiber content and 1300 V, the maximum fractal dimension reduction (11.52%) is observed in *S*1.5*P*0.5 during the increase in polypropylene fiber content from 0.25% to 0.5%.

In the present work, the parametric effects on the fractal dimension of SPFRC were clarified, and the intrinsic relationship between fracture energy dissipation and fractal characteristics was quantitatively revealed. The outcomes offer a reliable guideline for mixture optimization and impact toughness enhancement of hybrid fiber-reinforced concrete. Further research can be extended in the following aspects. First, advanced microscopic techniques including scanning electron microscopy and digital image correlation are recommended to characterize the microscale failure mechanism of SPFRC under dynamic impact. Establishing quantitative relationships between fractal parameters and microstructural features will advance the mixture design strategy from conventional macroscopic adjustment toward precise microscopic optimization. Second, future studies can focus on environmental adaptability by considering freeze–thaw damage and acid–alkali corrosion. Clarifying the coupling mechanism between external erosion, fractal evolution and energy dissipation behavior can provide a solid theoretical basis for the practical application of SPFRC in severe engineering environments. In addition, combined with specific engineering scenarios, life cycle economic cost analysis of hybrid fiber-reinforced concrete can be carried out, and a quantitative benchmarking system for performance improvement and cost increment can be established to provide a more comprehensive decision-making basis for engineering applications.

Author Contributions: Conceptualization, X.Y. and J.N.; Methodology, Q.Z.; Validation, B.W. and X.Z.; Formal analysis, B.W.; Investigation, B.W.; Data curation, Q.Z.; Writing—original draft, Q.Z.; Writing—review & editing, X.Y.; Visualization, J.N. and X.Z.; Supervision, X.Y. and X.Z. All authors have read and agreed to the published version of the manuscript.

Funding: This work was supported by the Henan Province University—Industry Collaborative Innovation Project (26AXQXT034) and Key Programs of Universities in Henan Province of China (25B560004).

Institutional Review Board Statement: Not applicable.

Informed Consent Statement: Not applicable.

Data Availability Statement: The data presented in this study are available on request from the corresponding author.

Conflicts of Interest: The authors declare no conflict of interest.

References

1. Wei, J.; Li, J.; Wu, C. An experimental and numerical study of reinforced conventional concrete and ultra-high performance concrete columns under lateral impact loads. *Eng. Struct.* **2019**, *201*, 109822. [CrossRef]
2. Qu, C.; Farzaneh, F.; Jung, S.; Zhang, Q. Strengthening reinforced concrete bridge piers against heavy vehicle collisions with ultra-high performance concrete collars: A finite element analysis study. *Adv. Struct. Eng.* **2024**, *27*, 1717–1733. [CrossRef]
3. Dhiman, P.; Kumar, V. Numerical investigation of reinforced concrete beams under impact loading. *Asian J. Civ. Eng.* **2024**, *25*, 537–554.
4. Zhang, X.G.; Wang, L.Y.; Shen, Y.C.; Liu, J.F.; Fan, Y.H. Analysis of flexural fatigue damage and micro-mechanisms of nano-SiO_2 modified recycled aggregate concrete. *Constr. Build. Mater.* **2025**, *487*, 142004. [CrossRef]
5. Bouzar, B.; Mamindy-Pajany, Y. Immobilization study of As, Cr, Mo, Pb, Sb, Se and Zn in geopolymer matrix: Application to shooting range soil and biomass fly ash. *Int. J. Environ. Sci. Technol.* **2023**, *20*, 11891–11912. [CrossRef]

6. Isojeh, B.; El-Zeghayar, M.; Vecchio, F.J. Fatigue behavior of steel fiber concrete in direct tension. *J. Mater. Civ. Eng.* **2017**, *29*, 04017130. [CrossRef]
7. Zhou, X.; Yang, Y.Y.; Li, X.Q.; Zhao, G.Q. Acoustic emission characterization of the fracture process in steel fiber reinforced concrete. *Comput. Concr. Int. J.* **2016**, *18*, 923–936. [CrossRef]
8. Cao, Q.; Zheng, H.; Ju, H.; Lin, Z.; Zhou, C.; Jia, J. Early-age cracking resistance of multiscale fiber-reinforced concrete with steel fiber, sisal fiber, and nanofibrillated cellulose. *J. Mater. Civ. Eng.* **2023**, *35*, 04023065. [CrossRef]
9. Huo, Z.P. Synthetic and properties analysis of the concrete composites doped with polypropylene fiber of different contents. *Fresennius Environ. Bull.* **2019**, *28*, 4627–4632.
10. Zhang, S.P.; Zhao, B.H. Influence of polypropylene fibre on the mechanical performance and durability of concrete materials. *Eur. J. Environ. Civ. Eng.* **2012**, *16*, 1269–1277. [CrossRef]
11. Xu, L.H.; Xu, H.R.; Chi, Y.; Zhang, Y. Experimental study on tensile strength of steel-polypropylene hybrid fiber reinforced concrete. *Adv. Sci. Lett.* **2011**, *4*, 911–916. [CrossRef]
12. Vinodkumar, M.; Muthukannan, M. Structural behaviour of HFRC beams retrofitted for shear using GFRP laminates. *Comput. Concr.* **2017**, *19*, 79–85. [CrossRef]
13. Xu, L.H.; Huang, L.; Chi, Y.; Mei, G.D. Tensile behavior of steel-polypropylene hybrid fiber-reinforced concrete. *ACI Mater. J.* **2016**, *113*, 219–229. [CrossRef]
14. Su, W.W.; Chen, Z.P.; Liao, H.Y.; Liu, D.Y.; Zhou, X.Y. Mechanical properties of steel-polypropylene fiber reinforced fully recycled coarse aggregate concrete. *Adv. Concr. Constr.* **2023**, *16*, 127–139.
15. Arsla, A. Mixed-mode fracture performance of fibre reinforced concrete under imPact loading. *Mater. Struct.* **1995**, *28*, 473–478. [CrossRef]
16. Ren, Z.G.; Chen, M.; Lu, Z.A.; Xu, W.G. Dynamic mechanical property of hybrid fiber reinforced concrete(HFRC). *J. Wuhan Univ. Technol.-Mater. Sci. Ed.* **2012**, *27*, 783–788. [CrossRef]
17. Guo, H.; Tao, J.L.; Chen, Y.; Li, D.; Jia, B.; Zhai, Y. Effect of steel and polypropylene fibers on the quasi-static and dynamic splitting tensile properties of high-strength concrete. *Constr. Build. Mater.* **2019**, *224*, 504–514. [CrossRef]
18. Song, P.S.; Wu, J.C.; Hwang, S.; Sheu, B.C. Statistical analysis of impact strength and strength reliability of steel-polypropylene hybrid fiber-reinforced concrete. *Constr. Build. Mater.* **2005**, *19*, 1–9. [CrossRef]
19. Guo, H.; Jiang, L.Z.; Tao, J.L.; Chen, Y.; Zheng, Z.Q.; Jia, B. Influence of a hybrid combination of steel and polypropylene fibers on concrete toughness. *Constr. Build. Mater.* **2021**, *275*, 122132. [CrossRef]
20. Li, F.; Luo, D.M.; Niu, D.T. Durability evaluation of concrete structure under freeze-thaw environment based on pore evolution derived from deep learning. *Constr. Build. Mater.* **2025**, *467*, 140422. [CrossRef]
21. Ng, K.; Sun, Y.; Dai, Q.L.; Yu, X. Investigation of internal frost damage in cementitious materials with micromechanics analysis, SEM imaging and ultrasonic wave scattering techniques. *Constr. Build. Mater.* **2014**, *50*, 478–485. [CrossRef]
22. Wu, H.L.; Zhang, Y.; Yao, K.S.; Yang, B. Failure process of steel-polypropylene hybrid fiber-reinforced concrete based on numerical simulations. *Sci. Eng. Compos. Mater.* **2022**, *29*, 299–311. [CrossRef]
23. Wang, Y.; Zhang, S.H.; Niu, D.T.; Fu, Q. Quantitative evaluation of the characteristics of air voids and their relationship with the permeability and salt freeze–thaw resistance of hybrid steel-polypropylene fiber-reinforced concrete composites. *Cem. Concr. Compos.* **2022**, *125*, 104292. [CrossRef]
24. Xu, L.H.; Wang, S.N.; Li, B.; Huang, L.; Chi, Y. An elastoplastic damage constitutive model for hybrid steel-polypropylene fiber reinforced concrete. *Int. J. Damage Mech.* **2022**, *31*, 1506–1532. [CrossRef]
25. Hou, Y.L.; Tie, Y.; Li, C.; Meng, L.; Sapanathan, T.; Rachik, M. On the damage mechanism of high-speed ballast impact and compression after impact for CFRP laminates. *Compos. Struct.* **2019**, *229*, 111435.
26. Prasad, N.; Murali, G. Exploring the impact performance of functionally-graded preplaced aggregate concrete incorporating steel and polypropylene fibres. *J. Build. Eng.* **2021**, *35*, 102077. [CrossRef]
27. Zhang, H.; Wei, D.M. Estimation of fracture toughness, driving force, and fracture energy for fractal cracks using the method of imaginary smooth crack. *Eng. Fract. Mech.* **2010**, *77*, 621–630. [CrossRef]
28. Yang, X.; Ma, S.; Dai, H.Z. Effect of geometric form of concrete meso-structure on its mechanical behavior under axial tension. *Constr. Build. Mater.* **2020**, *255*, 119295. [CrossRef]
29. Chen, M.; Cheng, J.H.; Zhang, T.; Wang, Y.T. Experimental characterization and constitutive modelling of the anisotropic dynamic compressive behavior of 3D printed engineered cementitious composites. *Cem. Concr. Compos.* **2025**, *160*, 105995. [CrossRef]
30. Erzar, B.; Forquin, P. Experiments and mesoscopic modelling of dynamic testing of concrete. *Mech. Mater.* **2011**, *43*, 505–527. [CrossRef]
31. Liu, H.F.; Liu, H.Y.; Song, W.D. Fracture characteristics of concrete subjected to impact loading. *Sci. China Phys. Mech. Astron.* **2010**, *53*, 253–261. [CrossRef]
32. Szeląg, M. Fractal characterization of thermal cracking patterns and fracture zone in low-alkali cement matrix modified with microsilica. *Cem. Concr. Compos.* **2020**, *114*, 103732. [CrossRef]

33. Pan, L.X.; Carrillo, J.; Cao, M.S.; Sha, G.G. Multifractal-spectrum shape parameters for characterizing distribution and evolution of multiple cracks in concrete structures. *Eng. Fract. Mech.* **2022**, *264*, 108329. [CrossRef]
34. Carpinteri, A.; Lacidogna, G.; Pugno, N. Structural damage diagnosis and life-time assessment by acoustic emission monitoring. *Eng. Fract. Mech.* **2007**, *74*, 273–289. [CrossRef]
35. Abdeldjalil, M.; Chouicha, K. Study of the prediction of the mechanical strength of concrete based on the fractal model of granular distribution. *Constr. Build. Mater.* **2022**, *348*, 128562. [CrossRef]
36. Carpinteri, A.; Accornero, F. Rotation versus curvature fractal scaling in bending failure. *Phys. Mesomech.* **2019**, *22*, 46–51. [CrossRef]
37. *GB 175-2023*; Common Portland Cement. China Architecture & Building Press: Beijing, China, 2023.
38. *GB/T 1596-2017*; Fly Ash Used for Cement and Concrete. China Architecture & Building Press: Beijing, China, 2017.
39. *GB/T 14685-2022*; Pebble and Crushed Stone for Construction. China Architecture & Building Press: Beijing, China, 2022.
40. *GB/T 14684-2022*; Sand for Construction. China Architecture & Building Press: Beijing, China, 2022.
41. *GB/T 39147-2020*; Steel Fiber for Concrete. China Architecture & Building Press: Beijing, China, 2020.
42. *GB/T 14337-2022*; Man-Made Fibre—Test Method for Tensile Properties of Staple Fibre. China Standards Press: Beijing, China, 2022.
43. *JGJ 55-2011*; Specification for Mix Proportion Design of Ordinary Concrete. Ministry of Housing and Urban-Rural Development of the People's Republic of China: Beijing, China, 2011.
44. *GB/T 50081-2019*; Standard for Test Methods of Concrete Physical and Mechanical Properties. China Architecture & Building Press: Beijing, China, 2019.
45. Rai, B.; Singh, N.K. Statistical and experimental study to evaluate the variability and reliability of impact strength of steel-polypropylene hybrid fiber reinforced concrete. *J. Build. Eng.* **2021**, *44*, 102937. [CrossRef]
46. Liu, W.; Liu, Y.S.; Wang, C.; Zhai, M.L. Study of fractal characteristics and energy release in rocks under impact loading. *KSCE J. Civ. Eng.* **2025**, *29*, 100101. [CrossRef]
47. Ren, W.B.; Xu, J.Y. Fractal characteristics of concrete fragmentation under impact loading. *J. Mater. Civ. Eng.* **2017**, *29*, 04016244. [CrossRef]
48. Turcotte, D.L. Fractals and fragmentation. *Geophys. Res.* **1986**, *91*, 1921–1926. [CrossRef]
49. Hassan, M.K. Multifractality and the shattering transition in fragmentation processes. *Phys. Rev. E* **1996**, *54*, 1126–1133. [CrossRef] [PubMed]
50. Zhang, H.; Ren, H.Q.; Mu, C.M.; Wu, X.Y.; Huang, K.; Zhang, H.E.; Wang, F. Experimental study on dynamic mechanical properties and damage characteristics of coral reef limestone. *Constr. Build. Mater.* **2023**, *384*, 131007. [CrossRef]
51. Luo, Y.; Li, S.H.; Gong, H.L.; Song, X.L.; Fan, R.; Zhang, J.R. Dynamic properties and fragmentation fractal characteristics of water-saturated reef limestone concrete under impact loading. *Constr. Build. Mater.* **2023**, *397*, 132417. [CrossRef]
52. Wang, T.J.; Xu, J.Y.; Bai, E.R.; Ren, B.; Lu, S. Coupling effects of axial static pressure ratio and high temperature on dynamic mechanical properties and crushing fractal characteristics of concrete under static-dynamic coupled loads. *J. Build. Eng.* **2022**, *59*, 105114. [CrossRef]
53. Xiong, Z.L.; Chen, X.D.; Fan, C.B.; Chen, N.; Shi, Z.Y. High strain rate dynamic behavior of autoclaved aerated concrete: Insights from Split Hopkinson Pressure Bar testing. *Constr. Build. Mater.* **2025**, *472*, 140968. [CrossRef]
54. Xie, F.X.; Jin, Z.H.; Yang, T.F.; Han, X.; Chen, X.D.; Zhang, Y. Experimental study of dynamic splitting-tensile properties of precast concrete samples under different strain rates. *Constr. Build. Mater.* **2023**, *372*, 130748. [CrossRef]
55. Yu, L.Y.; Peng, Y.X.; Li, W.; Zhang, T.; Ma, L.J.; Wu, D.Y.; Fan, D.D.; Zhou, L.J.; Hu, N.G. Experimental and numerical investigation of multiscale mechanical properties of coral aggregate seawater shotcrete. *Constr. Build. Mater.* **2024**, *450*, 138647. [CrossRef]
56. Li, S.Y.; Gao, Z.J.; Shao, Y.Z.; Gu, G.H. Impact resistance of hybrid steel fiber-reinforced concrete beam under accelerated non-uniform corrosion. *Buildings* **2026**, *16*, 1197. [CrossRef]
57. Cui, D.S.; Wang, L.M.; Zhang, C.W.; Xue, H.T.; Gao, D.W.; Chen, F.X. Dynamic splitting performance and energy dissipation of fiber-reinforced concrete under impact loading. *Materials* **2024**, *17*, 421. [CrossRef] [PubMed]
58. Gu, J.X.; Li, L.C.; Huang, X.; Chen, H. Study on shear performance of corroded steel fiber reinforced concrete beams under impact load. *Materials* **2024**, *17*, 2566. [CrossRef] [PubMed]
59. Li, J.Y.; Luo, J.W.; Chen, L.; Fan, X.M.; Zhu, Y.P.; Wang, X.Y.; Guo, J.P. Research on mechanical properties of steel-polypropylene fiber concrete and application of beam structure. *Front. Mater.* **2024**, *11*, 1440466. [CrossRef]
60. Wang, S.N.; Xu, L.H.; Chi, Y.; Cui, K.; Yin, C.R.; Li, B. Cyclic tensile behavior of ultra-high performance concrete with hybrid steel-polypropylene fiber: Experimental study and analytical model. *Compos. Struct.* **2023**, *321*, 117255. [CrossRef]
61. Jin, L.; Jia, L.K.; Zhang, R.B.; Yu, W.X.; Du, X.L. Mode-I fracture of steel fiber reinforced concrete at low temperatures: Characterization with 3D meso-scale modelling. *Theor. Appl. Fract. Mech.* **2023**, *124*, 103797. [CrossRef]
62. Chen, S.; Ma, X.; Lu, Y.; Luo, H.; Liangni. Bending behavior of fiber reinforced plastic (FRP) and steel fiber reinforced concrete beams. *Sci. Adv. Mater.* **2019**, *11*, 1037–1043. [CrossRef]

63. Perumal, R. Performance and modeling of high-performance steel fiber reinforced concrete under impact loads. *Comput. Concr.* **2014**, *13*, 255–270. [CrossRef]
64. Deng, F.Q.; Cao, C.; Xu, L.H.; Chi, Y. Interfacial bond characteristics of polypropylene fiber in steel/polypropylene blended fiber reinforced cementitious composite. *Constr. Build. Mater.* **2022**, *341*, 127897. [CrossRef]
65. Chen, L.J.; Zhang, X.X.; Liu, G.M. Analysis of dynamic mechanical properties of sprayed fiber-reinforced concrete based on the energy conversion principle. *Constr. Build. Mater.* **2020**, *254*, 119167. [CrossRef]
66. Zhang, K.J.; Lin, W.Q.; Lan, Q.B.; Zhang, Q.T. Compressive properties of polypropylene fiber reinforced seawater sea-sand recycled aggregate concrete under different strain rate loading. *Constr. Build. Mater.* **2024**, *452*, 138968. [CrossRef]
67. Singh, N.K.; Rai, B. Assessment of synergetic effect on microscopic and mechanical properties of steel-polypropylene hybrid fiber reinforced concrete. *Struct. Concr.* **2021**, *22*, 516–534. [CrossRef]
68. Gao, D.Y.; Yan, H.H.; Fang, D.; Yang, L. Bond strength and prediction model for deformed bar embedded in hybrid fiber reinforced recycled aggregate concrete. *Constr. Build. Mater.* **2020**, *265*, 120337. [CrossRef]
69. de Melo, F.M.C.; de Jesus Cruz, A.C.A.; de Souza Netto, L.D.; de Souza Simplício, M.A. Experimental study of bond between steel bars and hybrid fibers reinforced concrete. *Constr. Build. Mater.* **2021**, *275*, 122176. [CrossRef]
70. Zhang, X.G.; Li, M.B.; Niu, J.X.; Fan, Y.H.; Liu, J.F. Dynamic mechanical properties of steel-polypropylene hybrid fiber reinforced concrete. *Constr. Build. Mater.* **2025**, *485*, 141927. [CrossRef]
71. Zhang, X.G.; Li, Y.L.; Fan, Y.H.; Zhou, G.Q.; Huang, Y.J.; Xu, P.; Ding, Y.H. Analysis on the impact resistance of steel fiber reinforced recycled aggregate concrete. *Structures* **2025**, *75*, 108599. [CrossRef]
72. Xiong, Y.H.; Wen, Z.Y.; Zhang, L.Q.; Wen, Z.Q.; Liang, Y.Q. Application of fractal theory to spectral signal recognition. *Spectrosc. Spectr. Anal.* **2006**, *26*, 772–774.
73. Shi, F.; Pham, T.M.; Hao, H.; Hao, Y.F. Post-cracking behaviour of basalt and macro polypropylene hybrid fibre reinforced concrete with different compressive strengths. *Constr. Build. Mater.* **2020**, *262*, 120108. [CrossRef]
74. Liu, J.L.; Jia, Y.M.; Wang, J. Experimental study on mechanical and durability properties of glass and polypropylene fiber reinforced concrete. *Fibers Polym.* **2019**, *20*, 1900–1908. [CrossRef]

https://doi.org/10.3390/coatings16080910